Weierstraß-Institut
für Angewandte Analysis und Stochastik

im Forschungsverbund Berlin e.V.

Preprint ISSN 0946 – 8633

Optimizing the temperature profile during sublimation growth of SiC single crystals: Control of heating power, frequency, and coil position*

Christian Meyer[1], Peter Philip[2]

submitted: December 10, 2003

[1] Department of Mathematics
Technical University of Berlin
Straße des 17. Juni 136
D – 10623 Berlin
Germany
E-Mail: cmeyer@math.TU-Berlin.DE

[2] Weierstrass Institute
for Applied Analysis
and Stochastics
Mohrenstraße 39
D – 10117 Berlin
Germany
E-Mail: philip@wias-berlin.de

No. 895
Berlin 2003

2000 *Mathematics Subject Classification.* 80M50, 80A20, 65Z05, 65K10, 49-04.

Key words and phrases. Numerical simulation. Sublimation growth. Physical vapor transport. Modified Lely method. SiC single crystal. Nelder-Mead method. Optimization. RF heating.

1998 PACS numbers. 81.10.Bk, 02.60.Pn, 02.60.Cb, 44.05.+e, 84.32.Hh

* This work has been supported by the DFG Research Center "Mathematics for key technologies" (FZT 86) in Berlin and by the German Federal Ministry for Education and Research (BMBF) within the program "Neue Mathematische Verfahren in Industrie und Dienstleistungen" ("New Mathematical Methods in Manufacturing and Service Industry") # 03SPM3B5.

Edited by
Weierstraß-Institut für Angewandte Analysis und Stochastik (WIAS)
Mohrenstraße 39
10117 Berlin
Germany

Fax: + 49 30 2044975
E-Mail: preprint@wias-berlin.de
World Wide Web: http://www.wias-berlin.de/

Abstract

We use a numerical optimization method to determine the control parameters frequency, power, and coil position for the radio frequency (RF) induction heating of the growth apparatus during sublimation growth of SiC single crystals via physical vapor transport (PVT) (also called the modified Lely method). The control parameters are determined to minimize a functional, tuning the radial temperature gradient on the single crystal surface as well as the vertical temperature gradient between SiC source and seed, both being crucial for high-quality growth. The optimization is subject to constraints with respect to a required temperature difference between source and seed, a required temperature range at the seed, and an upper bound for the temperature in the entire apparatus. The numerical computations use a stationary mathematical model for the heat transport, including heat conduction, radiation, and RF heating to solve the forward problem, and a Nelder-Mead method for optimization. A minimal radial temperature gradient is found to coincide with a minimal temperature at the single crystal surface, and a maximal temperature gradient between source and seed is found to coincide with a low coil position.

1 Introduction

Silicon carbide (SiC) has numerous industrial applications, e.g. as a semiconductor substrate material in electronic and optoelectronic devices such as MESFETs, MOSFETs, thyristors, P-i-N diodes, Schottky diodes, blue and green LEDs, lasers, and sensors. SiC is especially suitable for use in high-temperature and intense-radiation environments. In spite of progress in the SiC growth technique, production of SiC devices is still limited by the lack of availability of large-diameter, low-defect SiC boules (cf. e.g. [MGH$^+$01, OFK$^+$02]).

SiC bulk single crystals are commonly grown by sublimation via the PVT method (modified Lely method [TT78, Kon95]). We consider an RF induction-heated PVT growth system, consisting of a graphite crucible containing polycrystalline SiC source powder and a single-crystalline SiC seed (see Fig. 1). The apparatus is heated to temperatures up to 3000 K, where the intended temperature at the SiC seed's surface can vary between 1900 and 3000 K, depending on the desired single crystal polytype to be grown [TT78, Kon95].

Initially, the growth cavity is filled with an inert gas, typically argon. The high temperatures then cause sublimation of SiC, adding species such as Si, Si_2C, and SiC_2 to the gas phase. To ensure SiC is transported from the source to the seed, the SiC source must be kept at a higher temperature than the SiC seed, such that sublimation is encouraged at the source and crystallization is encouraged at the seed. To that end, the source powder is placed in the hot zone of the growth apparatus, whereas the seed crystal is cooled by means of a blind hole.

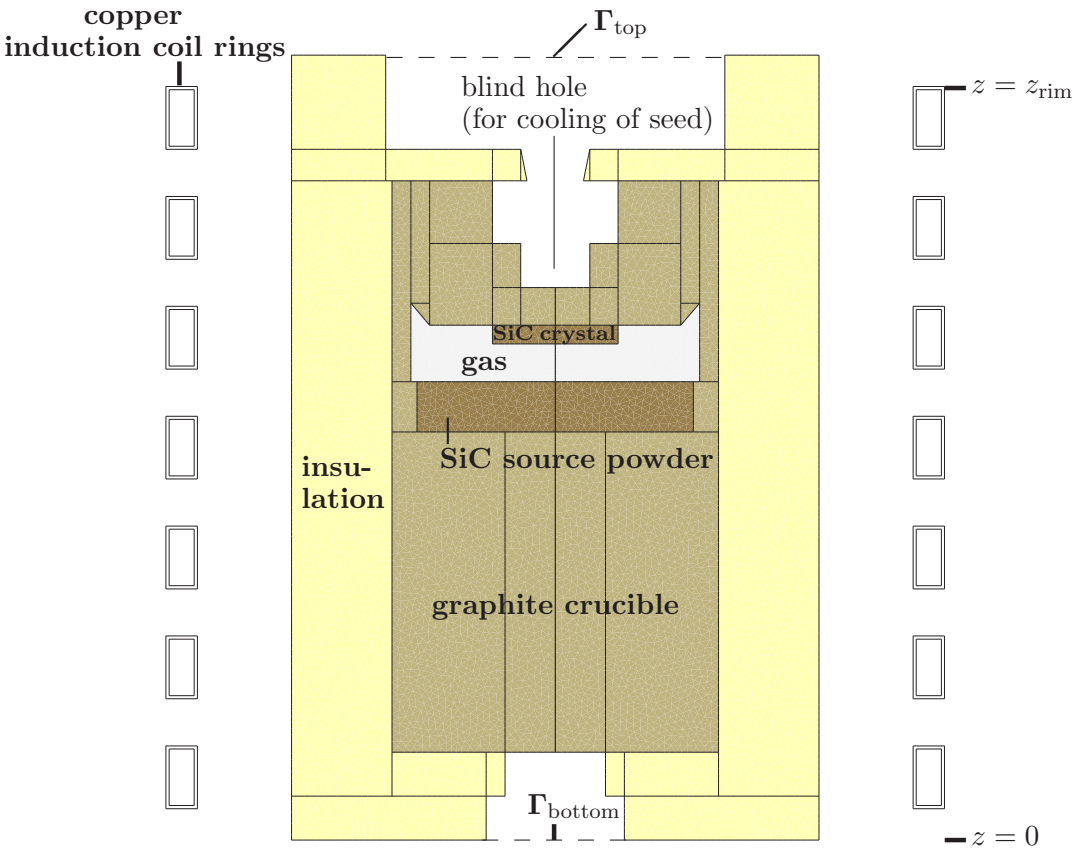

Figure 1: Setup of growth apparatus according to [PAC+99, Fig. 2].

The crystal's defect density and growth rate are strongly influenced by the temperature distribution (especially the temperature at the seed and the temperature difference between source and seed), the mass transport, and the pressure and concentrations of gas species [SBP98, RSD+99, SVK+00]. These *internal* control parameters can only be tuned indirectly by varying *external* control parameters such as the geometrical configuration of the setup, the power and frequency of the RF heater, the position of the induction coil, and the inert gas pressure.

Due to the high temperatures, measurements inside the growth chamber are extremely difficult and costly, and thus is the experimental optimization of the control parameters. Therefore, theoretical modeling and numerical methods play a fundamental role in improving growth conditions [PAC+99, KKZ+00, KP03, MZHS03, Phi03]. These and numerous other recent publications address the forward modeling of PVT growth. However, to the authors' knowledge, reports on optimization techniques applied to PVT growth are still scarce in the literature. An inverse finite-dimensional shape design problem to control the temperature at and temperature differences between finitely many prescribed points inside the powder source and inside the growth chamber has been solved in [KDK+01].

In the present paper, based on a stationary mathematical model for the heat transport in the growth system, we use numerical optimization to adjust the control parameters

power and frequency of the RF heater as well as the position of the induction coil such that the profile of the temperature field is optimized subject to an objective functional, controlling the radial temperature gradient at the seed crystal's surface as well as the vertical temperature gradient between source and seed.

The paper is organized as follows: We state the optimization problem in Sec. 2, including a brief description of the forward model. We describe our numerical methods in Sec. 3, and we present and discuss our numerical results in Sec. 4.

2 The Optimization Problem

Let $2\pi f$ be the angular frequency used for the induction heating with sinusoidal time dependence, let P be the prescribed effective total heating power, and let z_{rim} be the upper coil rim (s. Fig. 1).

We use (f, P, z_{rim}) as the control parameters of the considered optimization problem. If T denotes the absolute temperature in the growth system, then the forward problem consists of determining $T = T(f, P, z_{\mathrm{rim}})$ as the solution of a stationary heat transport problem described subsequently in this section. Keeping all other quantities fixed, T is indeed determined by (f, P, z_{rim}).

The optimization problem now lies in finding a triple

$$(\overline{f}, \overline{P}, \overline{z}_{\mathrm{rim}}) \in [f_{\min}, f_{\max}] \times [0, P_{\max}] \times [z_{\min}, z_{\max}] \tag{2.1}$$

such that a suitable objective functional $(f, P, z_{\mathrm{rim}}) \mapsto \mathcal{J}\big(T(f, P, z_{\mathrm{rim}})\big)$ becomes minimal at $(\overline{f}, \overline{P}, \overline{z}_{\mathrm{rim}})$, aiming at selecting a temperature field advantageous for the SiC growth process. The bounds of the intervals in (2.1) are called *box constraints* for the control parameters.

We consider an axisymmetric setting, i.e., in particular, we assume the growth apparatus as well as the temperature field to be cylindrically symmetric, merely depending on the cylindrical coordinates $(r, z) \in \Omega$, where Ω denotes the (2-dimensional) domain of the whole growth apparatus. Subsequently, we repeatedly need to calculate the maximum and minimum of functions defined on subsets of Ω. Hence, for $S \subseteq \Omega$, $f : S \longrightarrow \mathbb{R}$, we introduce

$$\max_S(f) := \max\big\{f(x) : x \in S\big\}, \quad \min_S(f) := \min\big\{f(x) : x \in S\big\}. \tag{2.2}$$

The best choice for the objective functional $\mathcal{J}(T)$ is not obvious, as the temperature field has to satisfy various conditions to support low-defect growth. For example, one aims at low radial temperature gradients on the growing crystal's surface to enable uniform growth under low thermal stress. One also needs to ensure a sufficiently large temperature difference between source and seed, where a larger temperature difference leads to a higher growth rate, but possibly also to a higher defect rate [MZPD02, Sec. 4], [SKM+00, Sec. 4].

In the present paper, we consider minimization of the objective functional

$$\mathcal{J}(T) = \mathcal{J}_\alpha(T) := \alpha \cdot \mathcal{F}_r(T) - (1-\alpha) \cdot \mathcal{F}_z(T), \quad T := T(f, P, z_{\text{rim}}), \tag{2.3}$$

where $\alpha \in [0,1]$ is a weight factor, and $\mathcal{F}_r$, $\mathcal{F}_z$ are suitable functionals measuring the size of the (absolute value of) radial and vertical gradient of T, respectively. Possible choices are the max-norm or the L_2-norm (cf. the numerical experiments in Sec. 4.2), where the corresponding versions of $\mathcal{F}_r$ read (s. (4.3) below for an L_2-version of $\mathcal{F}_z$):

$$\mathcal{F}_{r,\max}(T) := \max_\Gamma \left(\left| \frac{\partial T}{\partial r} \cdot \frac{\mathrm{m}}{\mathrm{K}} \right| \right), \quad \mathcal{F}_{r,2}(T) := \left(\int_\Gamma \frac{2\pi\, r}{\mathrm{m}} \left(\frac{\partial T}{\partial r}(r,z) \cdot \frac{\mathrm{m}}{\mathrm{K}} \right)^2 \frac{\mathrm{d}r}{\mathrm{m}} \right)^{\frac{1}{2}}, \tag{2.4}$$

where Γ denotes the horizontal lower surface of the SiC crystal (see Fig. 2). The units m and K occur in (2.4) as it will be convenient to keep the values of the objective functional unit-free.

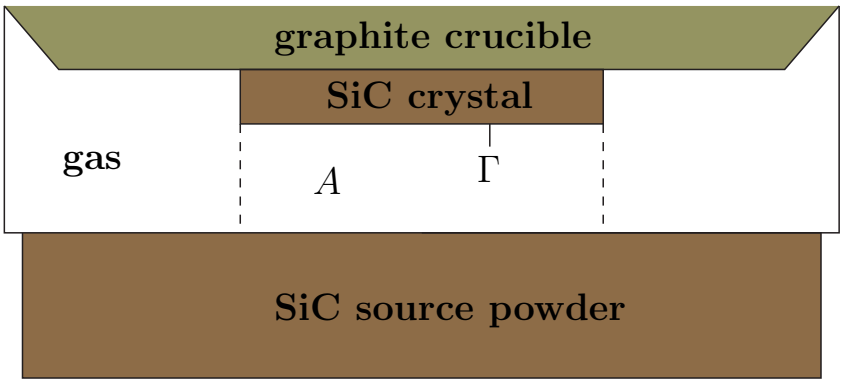

Figure 2: Enlargement of the reaction chamber of the setup depicted in Fig. 1.

The optimization is subject to a number of so-called *state constraints*: (a) The maximal temperature in the apparatus must not surpass a prescribed bound $T_{\max}$; (b) the temperature at the crystal surface needs to stay within a prescribed range $[T_{\min,\text{seed}}, T_{\max,\text{seed}}]$; (c) the temperature gradient between source and seed must be negative, and must not surpass a prescribed value $\Delta_{\max} < 0$. Thus, using the functionals (2.2), the state constraints can be formulated as

$$\max_\Omega(T) \le T_{\max}, \tag{2.5a}$$

$$T_{\min,\text{seed}} \le \min_\Gamma(T) \le \max_\Gamma(T) \le T_{\max,\text{seed}}, \tag{2.5b}$$

$$\max_A \left(\frac{\partial T}{\partial z} \right) \le \Delta_{\max} < 0, \tag{2.5c}$$

where A denotes the part of the gas domain directly underneath the SiC crystal (see Fig. 2). As (2.5c) ensures that $\frac{\partial T}{\partial z}$ is negative, the negative sign in front of the second term in (2.3) guarantees that the minimization (for small α) selects steeper negative vertical temperature gradients (encouraging faster mass transport from source to seed

and, thus, a higher growth rate). A large value of α means that the minimization stresses the objective of a flat radial temperature gradient. In Sections 4.2.2 and 4.2.3, we present results of numerical optimizations for both $\alpha = 1$ and $\alpha = 0.5$, where $\alpha = 0.5$ leads to a simultaneous optimization of both the radial and the vertical temperature gradient.

The numerical solution of the forward problem, i.e. the computation of the stationary temperature field $T(f, P, z_{\mathrm{rim}})$, requires a mathematical model of the heat transport mechanisms in the growth apparatus. We use the axisymmetric model for the temperature evolution in induction-heated PVT growth systems previously developed in [BKP+99, KPSW01, KP02, KP03]. We discard all time-dependent contributions, as, in the present article, we only consider the stationary final state. The model includes thermal conduction through solid materials as well as through the gas phase. Radiative heat transfer between surfaces of cavities is included using the net radiation method for diffuse-gray radiation as described in [KPSW01], where a band approximation model is used to account for the semi-transparency of the SiC single crystal. The growth apparatus is considered in a black body environment (e.g. a large isothermal room) radiating at room temperature T_{room}, such that outer boundaries emit according to the Stefan-Boltzmann law. For the two blind holes, we use black body phantom closures (denoted by Γ_{top} and Γ_{bottom} in Fig. 1) which emit radiation at T_{room}. We thereby allow for radiative interactions between the open cavities and the ambient environment, including reflections at the cavity surfaces.

Induction heating causes eddy currents in the conducting materials of the growth apparatus, resulting in heat sources due to the Joule effect. Assuming sinusoidal time dependence of the imposed alternating voltage, the heat sources are computed via an axisymmetric complex-valued magnetic scalar potential that is determined as the solution of an elliptic partial differential equation (PDE) (s. [KP03, Sec. 2]). To prescribe the total heating power, we follow [KP02, Sec. II], ensuring that the total current is the same in each coil ring.

Usually, during a physical growth run, the SiC source powder graphitizes and sinters, and chemical reactions inside the solid parts of the graphite crucible lead to changes in its porosity and can cause nonsealing joints. Moreover, accumulation of Si in the insulation felt is observed. It is not feasible to account for these changes at the current stage of numerical simulations. Hence, all simulations presented in this article are performed for an idealized growth apparatus, treating all solid materials as homogeneous and pure. Furthermore, it is assumed that the gas phase is made up solely of argon, which is a reasonable assumption for simulations of the temperature distribution [KPSW01, Sec. 5].

3 Numerical Methods

Our algorithm for determining view factors and shadowing during radiative heat transfer is based on [DNR+90] and is described in [KPSW01, Sec. 4]. A finite volume method

is used for the numerical solution of the linear elliptic PDEs arising from the magnetic scalar potential problem as well as for the numerical solution of the nonlinear elliptic PDEs governing the heat transfer. The resulting discrete nonlinear systems are solved by Newton's method.

The numerical solution of the above-described optimization problem, consisting of finding optimal control parameters (f, P, z_{rim}) that minimize the objective functional (2.3), is accomplished by the Nelder-Mead method [Kel99, Sec. 8.1.1]. The Nelder-Mead method constitutes a derivative-free method, i.e. the algorithm just needs the solution T of the heat transport problem as a function of the three control parameters (f, P, z_{rim}). This function is provided numerically using a finite volume approximation as explained above. The Nelder-Mead algorithm proceeds iteratively, aiming at reducing the objective functional in each step. More precisely, the Nelder-Mead algorithm starts with four initial values $(f_{\mathrm{i}_k}, P_{\mathrm{i}_k}, z_{\mathrm{rim},\mathrm{i}_k})$, $k \in \{1, \ldots, 4\}$, forming a simplex in the (f, P, z_{rim})-domain. In each iterative step, the simplex corner where the objective functional is worst is replaced such that a new simplex is formed. To enforce the box constraints (2.1), we proceed as follows: If (f, P, z_{rim}) as calculated by the current iteration of the Nelder-Mead method violates one (or more) of the box constraints (e.g. $f > f_{\max}$), then (f, P, z_{rim}) is projected back into the admissible domain (e.g. by replacing (f, P, z_{rim}) with $(f_{\max}, P, z_{\mathrm{rim}})$) before proceeding to the next iteration. To account for the state constraints (2.5), a penalty functional is introduced into the objective functional (2.3). Hence, the modified objective functional reads

$$\mathcal{J}_\alpha(T) = \alpha \cdot \mathcal{F}_r(T) - (1-\alpha) \cdot \mathcal{F}_z(T) + \sum_{i=1}^{4} \lambda_i \cdot \mathcal{H}_i(T),$$

where the $\mathcal{H}_i$ denote the penalty functionals corresponding to the different constraints, and the $\lambda_i \in \mathbb{R}^+$ are parameters that must be chosen sufficiently large to enforce the constraints. For instance, $\mathcal{H}_1(T) := \max\{0,\, \max_\Omega(T) - T_{\max}\}/\mathrm{K}$, and $\mathcal{H}_2$, $\mathcal{H}_3$, $\mathcal{H}_4$ are defined correspondingly. For each i, we found $\lambda_i = 50$ to be a suitable choice for our purposes.

All simulations were performed using the software *WIAS-HiTNIHS*[1] which is based on the program package *pdelib* [FKL01], and which uses the sparse matrix solver *Pardiso* [SGF00, SG03].

4 Numerical Results and Discussion

4.1 General Setting

We present numerical results for forward problems, computing stationary solutions $T(f, P, z_{\mathrm{rim}})$ given (f, P, z_{rim}) (s. Sec. 4.2.1), as well as numerical results for optimization problems, minimizing functionals $\mathcal{J}_\alpha\big(T(f, P, z_{\mathrm{rim}})\big)$ (s. Sec. 4.2.2 and Sec. 4.2.3). For all

[1] **Hi**gh **T**emperature **N**umerical **I**nduction **H**eating **S**imulator; pronunciation: ∼hit-nice.

Nelder-Mead optimization computations presented below, we use the box constraints (2.1) with

$$f_{\min} = 1 \text{ kHz}, \quad f_{\max} = 400 \text{ kHz}, \quad P_{\max} = 20 \text{ kW}, \quad z_{\min} = 8 \text{ cm}, \quad z_{\max} = 40 \text{ cm} \tag{4.1}$$

and the state constraints (2.5) with

$$T_{\max} = 3300 \text{ K}, \quad T_{\max,\text{seed}} = 3000 \text{ K}, \quad \Delta_{\max} = -\frac{10}{1.2}\frac{\text{K}}{\text{cm}} = -833.3\,\frac{\text{K}}{\text{m}}, \tag{4.2}$$

where $T_{\max}$ is chosen to avoid the destruction of the graphite crucible, $T_{\max,\text{seed}}$ is chosen according to the largest temperature values still being desirable for the growth of particular SiC polytypes [TT78, Kon95], and $\Delta_{\max}$ is chosen such that, if the vertical temperature gradient were constant between the SiC source powder and the single crystal, then the temperature of the source would always be at least 10 K above the temperature of the crystal. Concerning the state constraint $T_{\min,\text{seed}}$, we present results for both $T_{\min,\text{seed}} = 2500$ K and $T_{\min,\text{seed}} = 2300$ K.

All numerical computations presented in the following were performed for the growth system [PAC+99, Fig. 2] displayed in Fig. 1, consisting of an axisymmetric container having a radius of 8.4 cm and a height of 25 cm placed inside of 7 hollow rectangular-shaped copper induction rings. The geometric proportions of the coil rings are provided in Fig. 3.

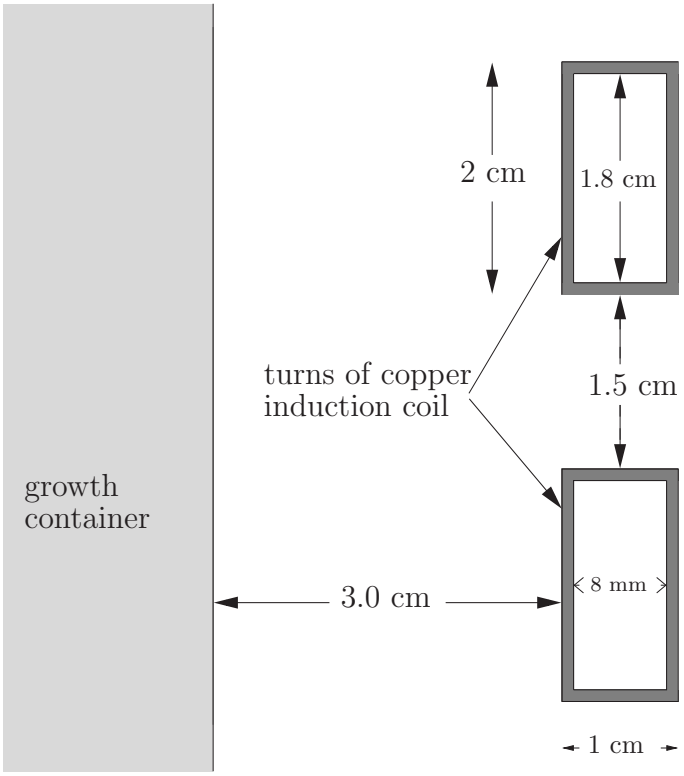

Figure 3: Geometric proportions of induction coil rings.

The material data used for the following numerical experiments are precisely the data provided in the appendices of [KPSW01] and [KP03], respectively.

4.2 Results

4.2.1 Forward Problem

In preparation of our discussion of optimization results presented subsequently in Sections 4.2.2 and 4.2.3, we investigate the form of the functional dependence $(f, P, z_{\mathrm{rim}}) \mapsto \mathcal{J}_\alpha\big(T(f, P, z_{\mathrm{rim}})\big)$, as well as the restrictions imposed by the constraints (2.5), by studying results of three series of forward computations. As before, $T(f, P, z_{\mathrm{rim}})$ denotes the solution of the stationary heat transfer problem given (f, P, z_{rim}). In each series, we compute $T = T(f, P, z_{\mathrm{rim}})$, keeping the frequency fixed (at $f = 5$ kHz, $f = 10$ kHz, $f = 20$ kHz, respectively), varying P between 5 and 12 kW in steps of 0.1 kW, and varying z_{rim} between 9 and 24 cm in steps of 1 mm.

For each solution, we compute the objective functional $\mathcal{J}_1(T) := \mathcal{F}_{r,2}(T)$ (cf. (2.4)) as well as the functionals $\max_A \left(\frac{\partial T}{\partial z}\right)(T)$, $\max_\Omega(T)$, $\min_\Gamma(T)$, and $\max_\Gamma(T)$ that are controlled by the state constraints (2.5). Interpolating the plotted functions bilinearly between the vertices of the rectangular P-z_{rim}-grid used for the computation series, the results are depicted in Figures 4 and 5. Figure 4 shows contour plots of $\mathcal{F}_{r,2}(T)$, restricted to the part of the (P, z_{rim})-plane where the state constraints given by (2.5) and (4.2) together with $T_{\mathrm{min,seed}} = 2300$ K (for Column (a)) and $T_{\mathrm{min,seed}} = 2500$ K (for Column (b)) are satisfied. For the 10-kHz-series, Fig. 5 depicts contour plots of the functionals $\max_A \left(\frac{\partial T}{\partial z}\right)(T)$, $\max_\Omega(T)$, $\min_\Gamma(T)$, and $\max_\Gamma(T)$, illustrating how the state constraints values chosen in (4.2), together with $T_{\mathrm{min,seed}} = 2300$ K or $T_{\mathrm{min,seed}} = 2500$ K, effect the domain restrictions in the (P, z_{rim})-plane.

In each case, we find that the admissible region in the (P, z_{rim})-plane constitutes a distorted triangle, where each side of the triangle corresponds to a cut-off caused by a state constraint. Comparing Columns (a) and (b) in Fig. 4 shows that the cut-off at the lower side of the triangular regions is due to $T_{\mathrm{min,seed}} \leq \min_\Gamma(T)$. Similarly, the upper side of the admissible regions is owing to $\max_A \left(\frac{\partial T}{\partial z}\right) \leq \Delta_{\max}$, and the right-hand side cut-off is caused by $\max_\Omega(T) \leq T_{\max}$, whereas, for the considered constraints values, $\max_\Gamma(T) \leq T_{\mathrm{max,seed}}$ has no restricting effect. For the 10-kHz-series, these findings are readily verified from Fig. 5.

For all three frequencies, Fig. 4 shows that, within each admissible region, $\mathcal{F}_{r,2}(T)$ increases with both P and z_{rim}. The same holds for the maximal and minimal temperatures at the crystal's surface (s. (3)(a), (3)(b) in Fig. 5), since the hot zone of the crucible is shifted upwards as z_{rim} increases. This dependence of the hot zone's location on z_{rim} also explains the results found in (1)(a) and (1)(b) of Fig. 5: The absolute value of the vertical temperature gradient between SiC source and crystal as measured by $\left|\max_A \left(\frac{\partial T}{\partial z}\right)\right|$ decreases with z_{rim} (Fig. 5(1)(a)), since, if the crucible's hot zone is further below the crystal, then the heat flux towards the crystal follows a vertical route, whereas it follows a more radial route if the crucible's hot zone is located more to the

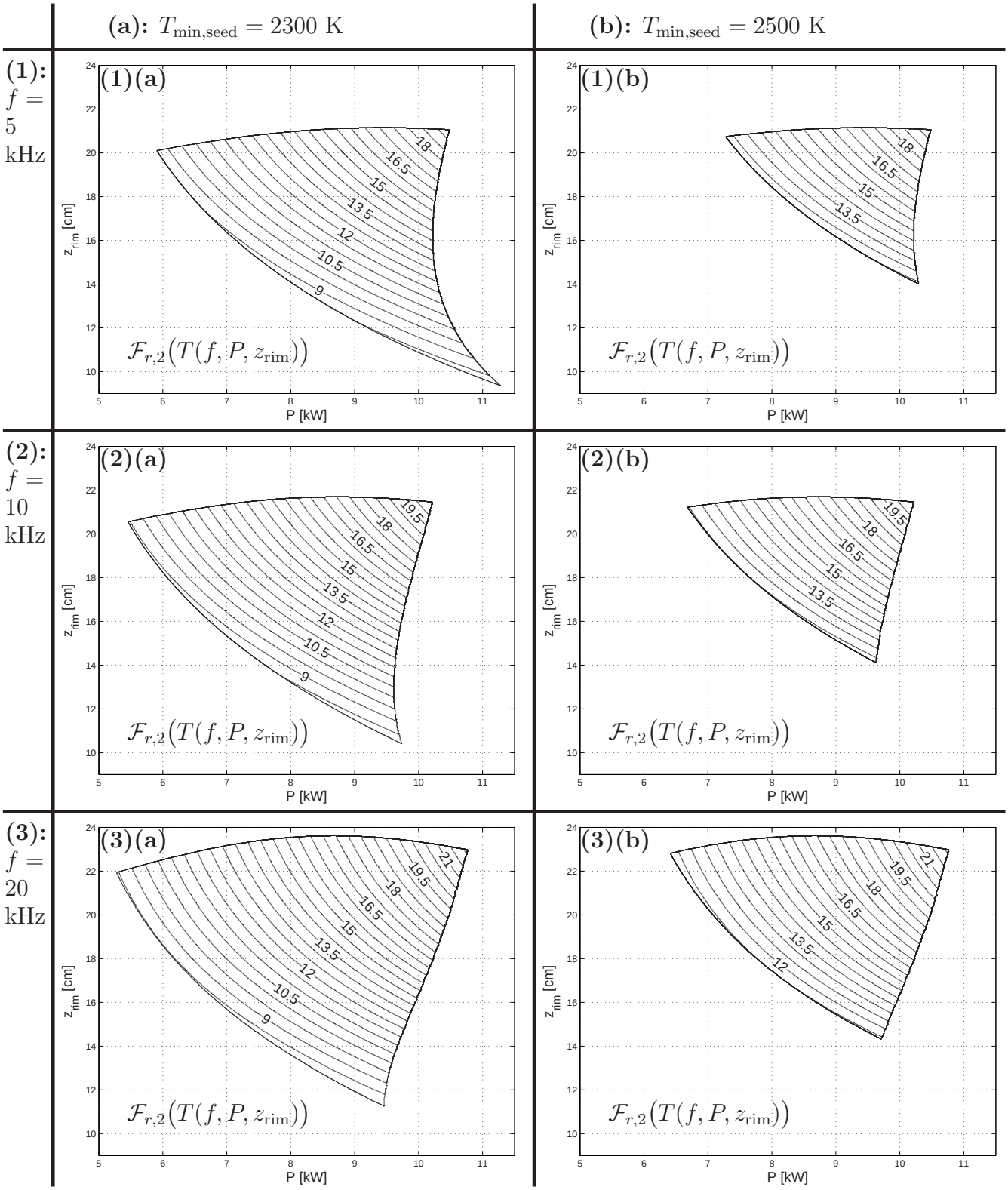

Figure 4: Contour plots of $\mathcal{F}_{r,2}\big(T = T(f,P,z_{\text{rim}})\big)$, T being the solution of the heat transfer problem, where f is kept fixed in each row. Each plot is restricted to the part of the (P, z_{rim})-plane where the state constraints given by (2.5) and (4.2) together with $T_{\min,\text{seed}} = 2300$ K (for Column (a)) and $T_{\min,\text{seed}} = 2500$ K (for Column (b)) are satisfied (cf. Fig. 5).

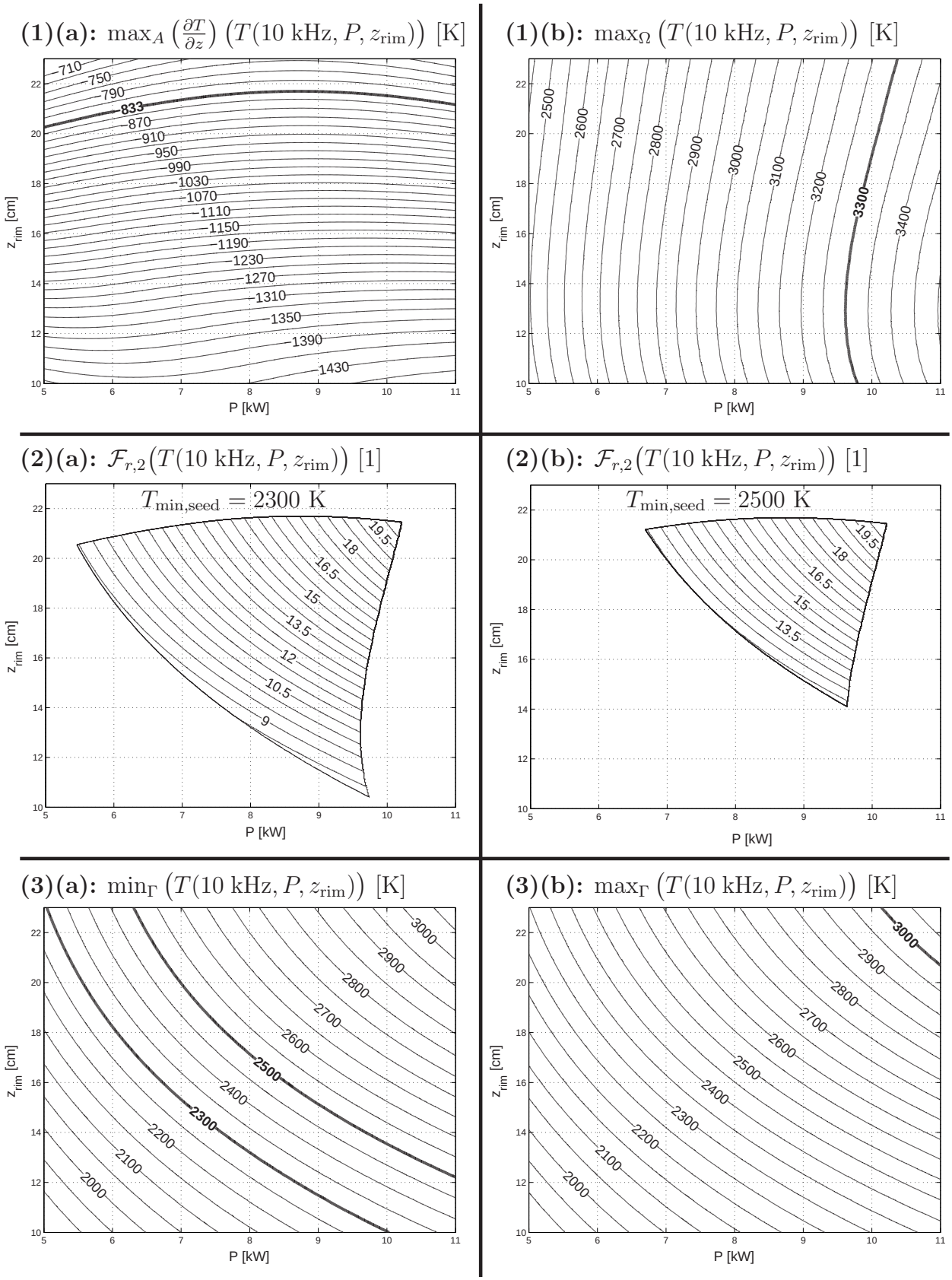

Figure 5: Illustration of state constraints (2.5) restricting the admissible (P, z_{rim})-domain: Contour plots of $\max_A \left(\frac{\partial T}{\partial z}\right)(T)$, $\max_\Omega(T)$, $\min_\Gamma(T)$, $\max_\Gamma(T)$ in Row (1); $\min_\Gamma(T)$, $\max_\Gamma(T)$ in Row (3); $\mathcal{F}_{r,2}(T)$ in Row (2); $T = T(f, P, z_{\text{rim}})$, $f = 10$ kHz, being the solution of the heat transfer problem. Values of used constraints are emphasized (cf. (4.2)).

side of the crystal. The maximal temperature in the apparatus $\max_\Omega(T)$ increases with P, but, for 10 cm $\leq z_{\rm rim} \leq$ 22 cm, as portrayed in Fig. 5(1)(b), it is almost independent of $z_{\rm rim}$ and the location of the hot zone.

Comparing the plots in Row 2 of Fig. 5 to those in Row 3 of Fig. 5 shows that the isolevels of $\mathcal{F}_{r,2}(T)$ are almost parallel to the isolevels of the maximal and minimal temperatures at the crystal's surface. This is further illustrated by the shapes of the lower cut-off edges of the admissible regions depicted in Fig. 4. Figure 4 also shows that, in general, $\mathcal{F}_{r,2}(T)$ does not depend monotonically on f, as, for fixed $(P, z_{\rm rim})$, the values for $\mathcal{F}_{r,2}(T)$ in Row 2 of Fig. 4 are slightly higher than the corresponding values in Rows 1 and 3 of Fig. 4.

4.2.2 2-Dimensional Optimization

In the current section, our main goal is to assess the performance and reliability of the Nelder-Mead method, when applied to the present optimization problem. We thus restrict the optimization to cases that were examined by forward computations such as discussed in the previous Sec. 4.2.1. Namely, we keep $f = 10$ kHz fixed, letting the Nelder-Mead method adjust P and $z_{\rm rim}$ to minimize the respective objective functional. Then, in the following Sec. 4.2.3, we proceed to the 3-dimensional case, where $(f, P, z_{\rm rim})$ all are determined by the Nelder-Mead method.

For the present 2-dimensional optimization, we consider four series of numerical experiments, using the Nelder-Mead method to minimize three different objective functionals, namely $\mathcal{J}_{1,2} := \mathcal{F}_{r,2}$, $\mathcal{J}_{1,\max} := \mathcal{F}_{r,\max}$, and $\mathcal{J}_{0.5,2} := \frac{1}{2}\mathcal{F}_{r,2} - \frac{1}{2}\mathcal{F}_{z,2}$, where $\mathcal{F}_{r,2}$ and $\mathcal{F}_{r,\max}$ were defined in (2.4), and

$$\mathcal{F}_{z,2}(T) := \left(\int_A \frac{2\pi\, r}{\rm m} \left(\frac{\partial T}{\partial z}(r,z) \cdot \frac{\rm m}{\rm K} \right)^2 \frac{{\rm d}(r,z)}{{\rm m}^2} \right)^{\frac{1}{2}} \tag{4.3}$$

is the L^2-norm of the vertical temperature gradient, computed over the region A between SiC source and seed (s. Fig. 2). As explained in Sec. 2, $\mathcal{J}_{0.5,2}$ favors a combination of a small radial temperature gradient and a large vertical temperature gradient to encourage mass transport from source to seed, increasing the growth rate.

Three optimization series are performed subject to the box constraints given by (2.1) and (4.1), and subject to the state constraints given by (2.5) and (4.2) completed with $T_{\rm min,seed} = 2500$ K. In the fourth optimization series, $\mathcal{J}_{0.5,2}$ is minimized using $T_{\rm min,seed} = 2300$ K, keeping all other constraints as before.

Each of the four series consists of 9 Nelder-Mead computations, varying the initial data $(P_{{\rm i}_k}, z_{{\rm rim},{\rm i}_k})$ (cf. description of Nelder-Mead method in Sec. 3 above). The results are displayed in Fig. 6, where, for each of the $4 \cdot 9$ Nelder-Mead computations, the found solution $(\overline{P}, \overline{z}_{\rm rim})$ is marked by a dot in the contour plot of the corresponding forward problem. Some solution values almost coincide, so that the corresponding dots can not be distinguished in the plots. Such multiple dots are marked by labeled arrows in the pictures.

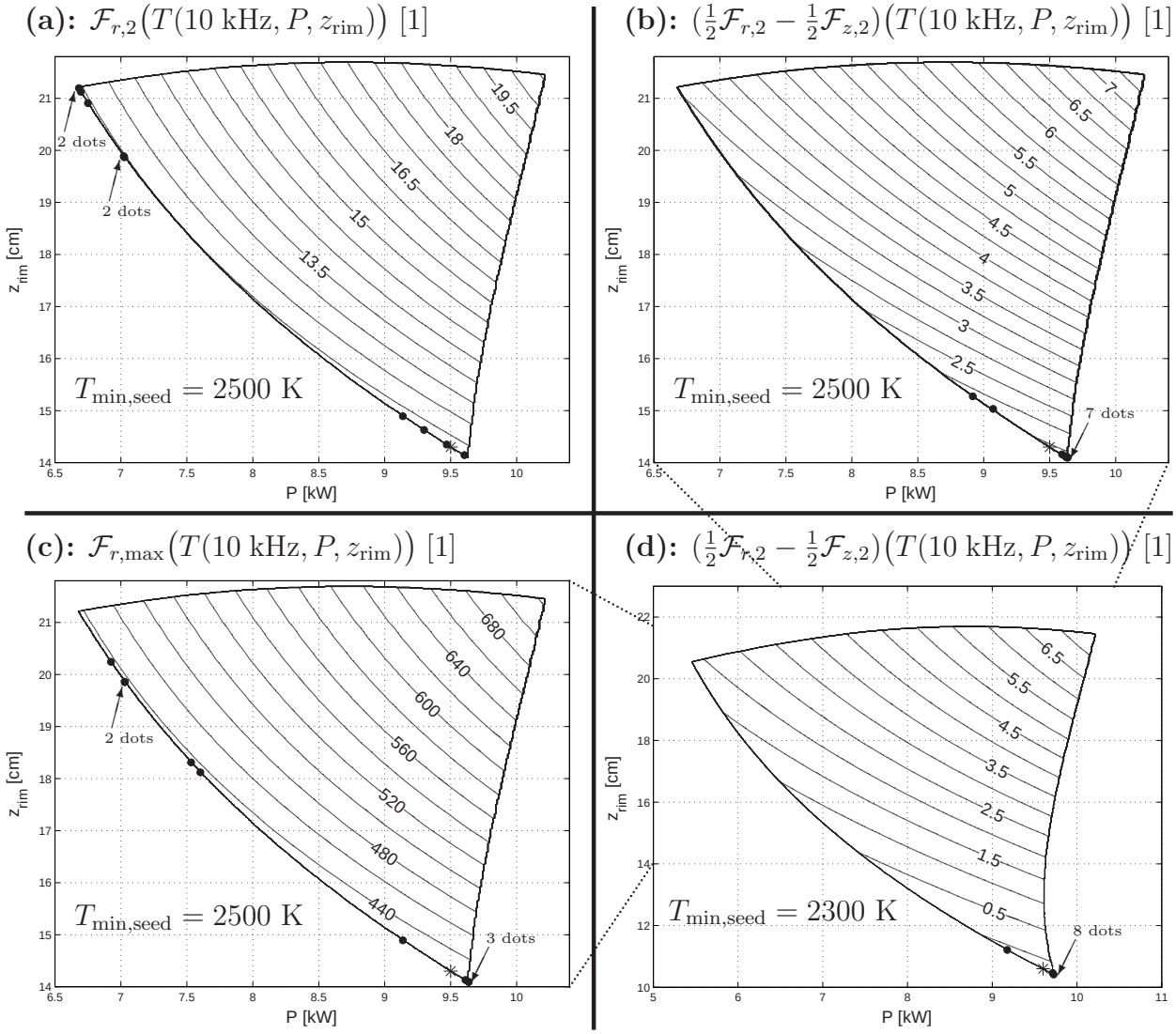

Figure 6: The locations of results of 2-dimensional Nelder-Mead computations (keeping $f = 10$ kHz fixed) is indicated in the contour plots of the respective minimized functional (dots on lower edge of respective admissible region). In each picture, a star marks the location where the smallest value of the considered objective functional occurred during the 10-kHz-series of forward computations discussed in Sec. 4.2.1. Plots (a), (b), (c) use $T_{\text{min,seed}} = 2500$ K, whereas plot (d) uses $T_{\text{min,seed}} = 2300$ K as well as a different P-z_{rim}-scale as indicated by the dotted lines.

It is seen in all four cases that, while every solution found by the Nelder-Mead method is located on the lower cut-off edge of the admissible region (determined by the constraint $T_{\text{min,seed}} \leq \min_\Gamma(T)$, cf. Sec. 4.2.1 above), the found solution is not unique, but depends on the initial data. This ambiguity in the found solutions is particularly prominent in Figures 6 (a) and (c), i.e. in the minimizations of $\mathcal{J}_{1,2}$ and $\mathcal{J}_{1,\max}$. Apparently, decreasing the objective functional, the Nelder-Mead algorithm follows the main gradient direction, which is virtually perpendicular to the lower edge of the corresponding admissible region, finally hitting the lower edge. However, as the objective functionals are almost constant parallel to the lower edge (even showing local minima at both ends of

the edge in Fig. 6 (a)), the Nelder-Mead method is, in general, not able to determine the absolute minimum on the lower edge.

The situation is somewhat better when minimizing $\mathcal{J}_{0.5,2}$ (s. Figures 6 (b) and (d)), where a distinct gradient is still present on the lower edges, with the absolute minimum at the lowermost corner (i.e. for maximal P and minimal z_{rim}). As indicated by the labeled arrows, in Fig. 6 (b), 7 out of 9 solutions are at the absolute minimum, and, likewise, 8 out of 9 solutions in Fig. 6 (d).

We note that the ambiguity in the found solutions is not that critical as, for all found solutions, the value of the objective functional is close to the absolute minimum as can be seen from both Fig. 6 and the following Tab. 1. Table 1 also compares the values of the objective functionals minimized by the Nelder-Mead method to the smallest value of the same functional that occurred during the 10-kHz-series of forward computations discussed in Sec. 4.2.1 above. The smallest value was attained at $(\overline{P}, \overline{z}_{\text{rim}})$ = (9.5 kW, 14.3 cm) for the computations depicted in Figures 6 (a) – (c), and at $(\overline{P}, \overline{z}_{\text{rim}})$ = (9.6 kW, 10.6 cm) for the computation depicted in Fig. 6 (d), where it is recalled that the series of forward computations were performed at steps of 0.1 kW and 0.1 cm, respectively. The respective location is marked by a star in Figures 6 (a) – (d). We note that one Nelder-Mead optimization took about 8 hours of computing time, whereas each forward computation took some 5 minutes, resulting in approximately 26 days for each row shown in Fig. 5.

Figure	Objective Functional $\mathcal{J}(T)$	Nelder-Mead: Range of $\mathcal{J}(T)$	Forward Problem: Best $\mathcal{J}(T)$
6 (a)	$\mathcal{J}_{1,2} := \mathcal{F}_{r,2}$	11.73 – 11.97	11.75
6 (b)	$\mathcal{J}_{0.5,2} := \frac{1}{2}\mathcal{F}_{r,2} - \frac{1}{2}\mathcal{F}_{z,2}$	1.917 – 2.153	1.958
6 (c)	$\mathcal{J}_{1,\max} := \mathcal{F}_{r,\max}$	422.2 – 436.7	423.4
6 (d)	$\mathcal{J}_{0.5,2} := \frac{1}{2}\mathcal{F}_{r,2} - \frac{1}{2}\mathcal{F}_{z,2}$	-0.194 – -0.08	-0.166

Table 1: Ranges of values of the objective functionals $\mathcal{J}(T)$ occurring in the solutions of the 2-dimensional Nelder-Mead optimizations considered in Fig. 6 compared to the best value of $\mathcal{J}(T)$ found in the corresponding forward computation.

We conclude that, in spite of the non-uniqueness in the found solutions due to the shape of the objective functionals on the admissible regions as determined by the state constraints, the Nelder-Mead algorithm effectively minimizes the objective functional in all considered cases.

Finally, we point out that Figures 6 (b) and (d) reveal that the behavior of the functional $\mathcal{J}_{0.5,2}$ is similar to that shown by $\mathcal{F}_{r,2}$, as its value also increases with both P and z_{rim}. However, the isolevels of $\mathcal{J}_{0.5,2}$ are no longer quite parallel to the isolevels of $\min_\Gamma(T)$. On the other hand, comparing Figures 6 (a) and (c) shows that the behavior of $\mathcal{F}_{r,2}$ and $\mathcal{F}_{r,\max}$ is almost identical.

4.2.3 3-Dimensional Optimization

For each of the four series of 2-dimensional Nelder-Mead optimizations considered in the previous Sec. 4.2.2, we conducted a corresponding series of 3-dimensional Nelder-Mead optimizations, controlling f in addition to P and z_{rim}. As in Sec. 4.2.2, we minimize the objective functionals $\mathcal{J}_{1,2}$, $\mathcal{J}_{1,\max}$, and $\mathcal{J}_{0.5,2}$ subject to the box constraints given by (2.1) and (4.1) (now also relevant for f) and the state constraints given by (2.5) and (4.2) together with $T_{\text{min,seed}} = 2500$ K. For $\mathcal{J}_{0.5,2}$, we also consider $T_{\text{min,seed}} = 2300$ K. In a new fifth series, we also minimize $\mathcal{J}_{1,2}$ using $T_{\text{min,seed}} = 2300$ K. In each series, we have 27 Nelder-Mead computations, varying the initial values $(f_{\text{i}}, P_{\text{i}}, z_{\text{rim,i}})$. As explained in Sec. 3 above, each Nelder-Mead computation actually needs *four* initial values, and we generate the remaining three by successively replacing f_{i}, P_{i}, $z_{\text{rim,i}}$ by a smaller value: f_{i} is replaced by $\max\{f_{\min}, f_{\text{i}} - 0.2 \cdot (f_{\min} + f_{\max})\}$, and P_{i} and $z_{\text{rim,i}}$ are replaced analogously.

For each series, the 5 results with the smallest values for the objective functional $\mathcal{J}(T)$ and the result with the largest value for $\mathcal{J}(T)$ are collected in a table (Tables 2 – 6 below).

f_{i} [kHz]	P_{i} [kW]	$z_{\text{rim,i}}$ [cm]	$\overline{f}$ [kHz]	$\overline{P}$ [kW]	$\overline{z}_{\text{rim}}$ [cm]	$\mathcal{J}_1(T)$ [1]	$\max_\Omega(T)$ [K]	$\min_\Gamma(T)$ [K]	$\max_\Gamma(T)$ [K]	$\max_A\left(\frac{\partial T}{\partial z}\right)$ [K/m]
400	5	28	248	11.4	23.9	358	2637	2500	2505	- 841.6
100	15	16	152	9.35	23.9	359	2631	2500	2505	- 839.4
100	15	32	282	12.3	23.5	360	2655	2500	2505	- 866.4
100	5	16	127	8.76	23.8	361	2632	2500	2505	- 847.3
400	15	32	399	14.4	23.3	361	2672	2500	2505	- 894.0
10	15	24	10.6	7.68	17.9	434	2957	2500	2506	-1058

Table 2: Optimal parameters and functional values as computed by the Nelder-Mead method for $T_{\text{min,seed}} = 2500$ K, $\alpha = 1$, $\mathcal{J}_1 = \mathcal{F}_{r,\max}$.

f_{i} [kHz]	P_{i} [kW]	$z_{\text{rim,i}}$ [cm]	$\overline{f}$ [kHz]	$\overline{P}$ [kW]	$\overline{z}_{\text{rim}}$ [cm]	$\mathcal{J}_1(T)$ [1]	$\max_\Omega(T)$ [K]	$\min_\Gamma(T)$ [K]	$\max_\Gamma(T)$ [K]	$\max_A\left(\frac{\partial T}{\partial z}\right)$ [K/m]
400	10	24	314	12.7	24.1	9.80	2630	2500	2505	- 834.1
400	15	24	400	14.2	24.1	9.81	2628	2500	2505	- 838.5
400	5	32	332	13.1	24.0	9.82	2633	2500	2505	- 840.4
100	5	32	161	9.57	24.0	9.85	2630	2501	2506	- 835.6
100	10	32	182	10.1	23.6	9.86	2647	2500	2505	- 857.1
10	5	24	5.34	8.93	16.1	12.1	3128	2500	2506	-1130

Table 3: Optimal parameters and functional values as computed by the Nelder-Mead method for $T_{\text{min,seed}} = 2500$ K, $\alpha = 1$, $\mathcal{J}_1 = \mathcal{F}_{r,2}$.

We still find that, for all computed solutions, $\min_\Gamma(T)$ is close to the minimal admissible value, (2500 K in Tables 2 – 4, 2300 K in Tables 5 and 6). This corresponds to the fact that all solutions found during the 2-dimensional computations of Sec. 4.2.2 were

f_i [kHz]	P_i [kW]	$z_\mathrm{rim,i}$ [cm]	$\overline{f}$ [kHz]	$\overline{P}$ [kW]	$\overline{z}_\mathrm{rim}$ [cm]	$\mathcal{J}_{0.5}(T)$ [1]	$\mathcal{F}_{r,2}(T)$ [1]	$\max_\Omega(T)$ [K]	$\min_\Gamma(T)$ [K]	$\max_\Gamma(T)$ [K]	$\max_A\left(\frac{\partial T}{\partial z}\right)$ [K/m]
400	15	16	280	16.4	16.1	1.18	10.6	3299	2500	2505	-1343
100	10	24	84.5	10.9	15.6	1.19	10.7	3289	2500	2505	-1366
100	15	24	186	13.9	16.1	1.19	10.6	3283	2500	2505	-1344
400	15	32	393	19.0	16.0	1.19	10.6	3294	2500	2505	-1341
400	15	24	390	19.0	16.0	1.19	10.6	3299	2501	2506	-1342
10	15	24	10.2	8.53	16.0	2.29	11.8	3114	2500	2506	-1177

Table 4: Optimal parameters and functional values as computed by the Nelder-Mead method for $T_\mathrm{min,seed} = 2500$ K, $\alpha = 0.5$, $\mathcal{J}_{0.5} = \frac{1}{2}\mathcal{F}_{r,2} - \frac{1}{2}\mathcal{F}_{z,2}$.

f_i [kHz]	P_i [kW]	$z_\mathrm{rim,i}$ [cm]	$\overline{f}$ [kHz]	$\overline{P}$ [kW]	$\overline{z}_\mathrm{rim}$ [cm]	$\mathcal{J}_1(T)$ [1]	$\max_\Omega(T)$ [K]	$\min_\Gamma(T)$ [K]	$\max_\Gamma(T)$ [K]	$\max_A\left(\frac{\partial T}{\partial z}\right)$ [K/m]
100	10	16	165	7.98	22.7	7.47	2459	2300	2304	- 845.8
400	5	16	273	10.2	21.4	7.54	2526	2300	2304	- 940.9
400	10	16	337	11.8	19.8	7.62	2611	2300	2304	-1054
100	15	24	216	10.0	19.2	7.64	2656	2300	2304	-1099
100	5	32	106	7.16	20.9	7.65	2538	2301	2305	- 977.0
10	15	32	2.85	8.87	15.6	8.88	2863	2300	2304	-1128

Table 5: Optimal parameters and functional values as computed by the Nelder-Mead method for $T_\mathrm{min,seed} = 2300$ K, $\alpha = 1$, $\mathcal{J}_1 = \mathcal{F}_{r,2}$.

f_i [kHz]	P_i [kW]	$z_\mathrm{rim,i}$ [cm]	$\overline{f}$ [kHz]	$\overline{P}$ [kW]	$\overline{z}_\mathrm{rim}$ [cm]	$\mathcal{J}_{0.5}(T)$ [1]	$\mathcal{F}_{r,2}(T)$ [1]	$\max_\Omega(T)$ [K]	$\min_\Gamma(T)$ [K]	$\max_\Gamma(T)$ [K]	$\max_A\left(\frac{\partial T}{\partial z}\right)$ [K/m]
100	5	32	84.9	10.3	12.9	-0.520	7.71	3296	2300	2304	-1467
100	5	16	72.9	10.0	12.7	-0.517	7.73	3299	2301	2304	-1471
100	10	16	66.8	9.86	12.7	-0.509	7.75	3291	2300	2304	-1471
100	10	24	87.7	10.3	13.0	-0.508	7.71	3291	2301	2304	-1465
100	10	32	155	12.1	13.3	-0.508	7.66	3295	2300	2304	-1456
10	15	32	3.37	12.5	10.0	0.014	8.33	3225	2300	2304	-1396

Table 6: Optimal parameters and functional values as computed by the Nelder-Mead method for $T_\mathrm{min,seed} = 2300$ K, $\alpha = 0.5$, $\mathcal{J}_{0.5} = \frac{1}{2}\mathcal{F}_{r,2} - \frac{1}{2}\mathcal{F}_{z,2}$.

located on the lower edge of the admissible region (cf. Fig. 6), recalling that the lower edge was determined by the minimal admissible value for $\min_\Gamma(T)$ (cf. Fig. 5).

Moreover, the ambiguity in the found solutions observed during the 2-dimensional optimizations is also present in the 3-dimensional results. Comparing the values for $\mathcal{J}(T)$ in Tables 2 – 6 with the corresponding values in Tab. 1, we find that the best values found in the 2-dimensional optimizations at $f = 10$ kHz are usually close to the least favorable values found in the corresponding 3-dimensional optimizations, while the best values are considerably improved in the 3-dimensional case. Except for the series minimizing $\mathcal{J}_{1,2}$ with $T_\mathrm{min,seed} = 2300$ K (Tab. 6), the best values of $\mathcal{J}(T)$ correspond to

frequencies $\overline{f}$ over 100 kHz (4-th column of Tables 2 – 6).

In Sec. 4.2.2, keeping $f = 10$ kHz fixed, we found that increasing P and z_{rim} increased both the temperature at the SiC crystal's surface Γ and the objective functionals. On the other hand, the temperature at Γ and the objective functionals were decreased when raising f from 10 kHz to values over 100 kHz due to an intensified skin effect: As the frequency rises, the heat sources are concentrated in an ever thinner region of the graphite crucible, reducing the efficiency of the heat transport to the crystal. This explains that, in each of the Tables 2 – 6, where the single crystal's temperature is virtually constant within each table, a higher frequency $\overline{f}$ corresponds to either a higher power $\overline{P}$ or a higher coil position $\overline{z}_{\text{rim}}$.

Examining the values of $\overline{z}_{\text{rim}}$ in Column 6 of Tables 2 – 4 and 6 reveals that in four of the five series, the variation in $\overline{z}_{\text{rim}}$ among the five best results is much less than the corresponding variation in $\overline{f}$ and $\overline{P}$. This indicates that the shape of the isotherms inside the gas phase as measured by the considered objective functionals is tuned more effectively by adjusting the coil position than by controlling power or frequency. Moreover, the values for $\overline{z}_{\text{rim}}$ are considerably lower in Tables 4 and 6 (where $\alpha = 0.5$) than in Tables 3 and 5 (where $\alpha = 1$). Recalling that $\alpha = 0.5$ means that the objective functional has one contribution $\mathcal{F}_{r,2}(T)$ to minimize the radial temperature gradient and one contribution $-\mathcal{F}_{z,2}(T)$ to maximize the absolute value of the vertical temperature gradient, it is seen that a lower coil position is advantageous for maximizing $\mathcal{F}_{z,2}(T)$, as was already noted when evaluating Fig. 5(1)(a) in Sec. 4.2.1 above.

In Tables 4 and 6, where $\alpha = 0.5$, an additional column is provided, displaying the radial contribution $\mathcal{F}_{r,2}(T)$ (Column 8). Comparing the values for $\mathcal{F}_{r,2}(T)$ in Tab. 3 with those for $\mathcal{J}_1(T) = \mathcal{F}_{r,2}(T)$ in Tab. 4 (Row 1: $\mathcal{F}_{r,2}(T)$ equals 9.80 and 10.6, respectively) and, analogously, for Tables 5 and 6 (Row 1: $\mathcal{F}_{r,2}(T)$ equals 7.47 and 7.71, respectively), demonstrates only a small increase in the radial gradient for $\alpha = 0.5$. At the same time, comparing the vertical gradients for the best results as measured by $\max_A \left(\frac{\partial T}{\partial z}\right)$ (last column in each table) shows that optimization of $\mathcal{J}_{0.5}(T)$ increases the absolute value of the vertical gradient by more than 50 percent (Row 1, Tables 3 and 4: $\max_A \left(\frac{\partial T}{\partial z}\right)$ equals -834.1 K/m and -1343 K/m, respectively; Row 1, Tables 3 and 4: $\max_A \left(\frac{\partial T}{\partial z}\right)$ equals -845.8 K/m and -1467 K/m, respectively). In this context, we also observe that, for $\alpha = 1$, the best optimization results all show a value for $\max_A \left(\frac{\partial T}{\partial z}\right)$ that is close to the largest admissible value of -833.3 K/m (first row of Tables 2, 3, and 5). A similar behavior was *not* present in our 2-dimensional optimization results depicted in Fig. 6, where the upper edge of each triangular region corresponds to $\max_A \left(\frac{\partial T}{\partial z}\right) =$ -833.3 K/m, but the optimization results were, in general, not close to the upper edge.

Summarizing the results of the previous paragraph, we conclude that the radial and the vertical gradient can be effectively tuned simultaneously.

The effect of the respective minimizations of $\mathcal{J}_1(T) := \mathcal{F}_{r,2}(T)$ and of $\mathcal{J}_{0.5}(T) := \frac{1}{2}\mathcal{F}_{r,2}(T) - \frac{1}{2}\mathcal{F}_{z,2}(T)$ on the shape of the temperature distribution between SiC source and crystal, is portrayed in Fig. 7. In Fig. 7(a), one has the stationary solution for a generic, unoptimized situation, using $f = 10$ kHz, $P = 10$ kW, and $z_{\text{rim}} = 24$ cm (i.e. the coil position of Fig. 1). Figures 7(b) and (c) display the solutions with the lowest

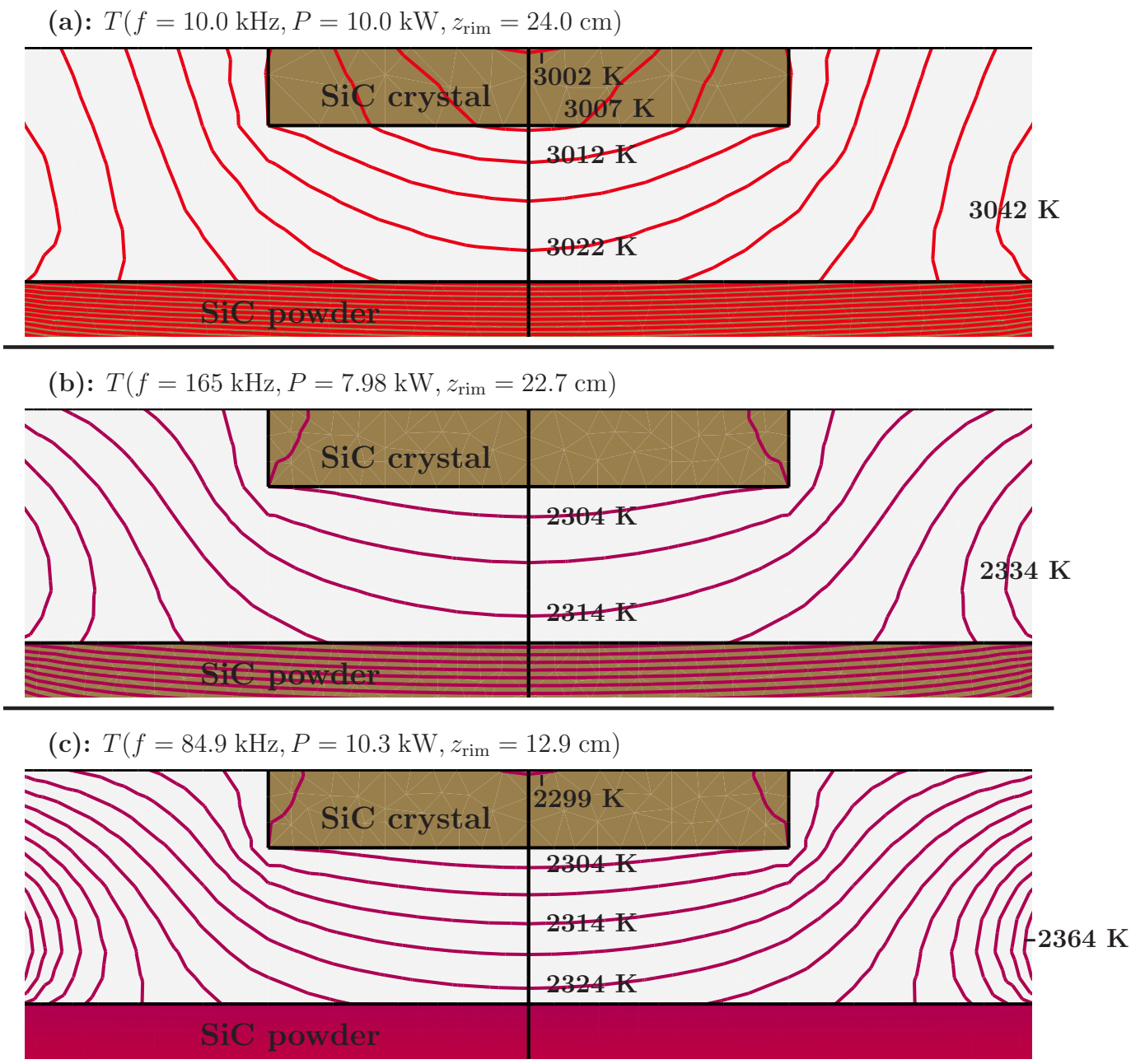

Figure 7: The stationary solution for the temperature field $T(f, P, z_{\text{rim}})$ is portrayed inside the gas phase between SiC source and SiC crystal for three different choices of (f, P, z_{rim}): (a) is a generic, unoptimized situation, z_{rim} being as in Fig. 1; (b) and (c) show results of Nelder-Mead optimizations, where $\mathcal{J}_1 = \mathcal{F}_{r,2}$ was minimized for (b) and $\mathcal{J}_{0.5} = \frac{1}{2}\mathcal{F}_{r,2} - \frac{1}{2}\mathcal{F}_{z,2}$ was minimized for (c) (cf. first rows of Tables 5 and 6, respectively). In each picture, the isotherms are spaced at 5 K, and they are chosen such that one isotherm passes through the lower outer corner of the SiC crystal.

values for $\mathcal{J}_1(T)$ and $\mathcal{J}_{0.5}(T)$, respectively, found by the 3-dimensional Nelder-Mead computations (cf. first rows of Tables 5 and 6, respectively).

The main difference between the generic solution of Fig. 7(a) and the optimized solutions shown in Figures 7(b),(c) is the gained homogeneity of the temperature inside the SiC crystal in the optimized solutions (favorable with respect to low thermal stress and few crystal defects) as well as the isotherms below the crystal's surface becoming more parallel to that surface (as intended by the minimization of $\mathcal{F}_{r,2}$). As expected, in Fig. 7(c), the maximization of $\mathcal{F}_{z,2}$ leads to an increased number of isotherms between the crystal and the source powder, having the desirable side effect of flattening the isotherms further.

Finally, to provide an impression of the performance of the Nelder-Mead method as applied during the computations presented above, in Fig. 8, we have plotted the best value of the objective functional depending on the number of iterations for four different numerical optimizations. As explained in Sec. 3, in each iterative step of the Nelder-Mead method, one of four points that constitute the corners of a simplex in the (f, P, z_{rim})-domain is replaced. More precisely, the point with the largest value for the objective functional is replaced, aiming at finding a new point where the value is lower. However, in general, it occurs that the new value is not lower than all values corresponding to the points that were kept fixed, resulting in the plateaus present in Fig. 8. The initial data for Figures 8(1)(a),(b) correspond to the first row of Tab. 2, whereas the initial data for Figures 8(2)(a),(b) correspond to the first row of Tab. 3.

We found that, in most cases, the Nelder-Mead method converged rapidly as depicted in Fig. 8. However, we note that, in a few cases, letting n denote the number of iterations, we observed a slower convergence due to $(f(n), P(n), z_{\mathrm{rim}}(n))$ drifting in and out of the admissible region at the boundary defined by $T_{\mathrm{min,seed}} \leq \min_{\Gamma}(T)$.

Comparing Fig. 8(1)(a) with Fig. 8(1)(b) and Fig. 8(2)(a) with Fig. 8(2)(b), it can be seen that the minimization of the max-norm and of the L^2-norm of the radial temperature gradient show an almost identical convergence behavior.

5 Conclusions

We used a stationary numerical model for the heat transfer in induction-heated PVT growth systems, to numerically optimize the temperature field in the gas phase between SiC source powder and single crystal, controlling frequency and power of the induction coil as well as the coil position. The numerical optimization was accomplished employing the Nelder-Mead method that was shown to be effective in minimizing the radial temperature gradient at the crystal's surface and in simultaneously maximizing the absolute value of the vertical temperature gradient between SiC source and crystal. However, ambiguous solutions occur due to flat regions and local minima of the considered objective functionals.

Our results indicate that the shape of the isotherms inside the gas phase as measured by the considered objective functionals is tuned more effectively by adjusting the coil position than by controlling power or frequency, where the maximal absolute value for the vertical temperature gradient between source and seed was achieved for a low coil

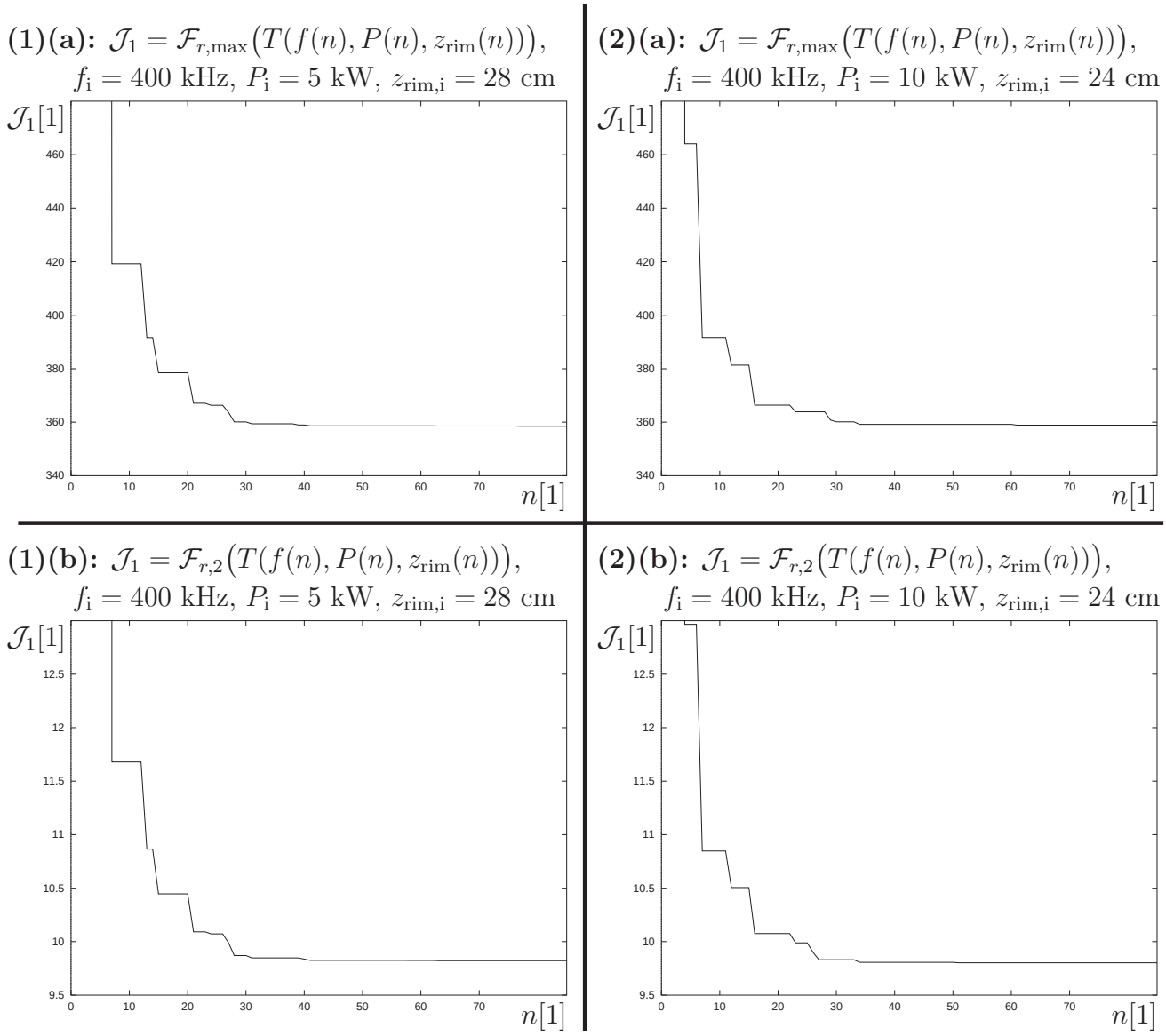

Figure 8: Comparison of convergence rate of Nelder-Mead method for two different objective functionals and two choices of initial data: In each case, the value of the best objective functional $\mathcal{J}_1$ is depicted as a function of the number of iterations n.

position.

Furthermore, the minimal radial temperature gradient at the crystal's surface always occurred for a temperature distribution that established the lowest admissible temperature at the crystal's surface. We thus conclude that it might be desirable to grow SiC single crystals at the lowest possible temperature in view of reducing radial thermal stress. This dovetails well with the original findings of [TT78, Sec. 3], where a low growth temperatue was found to be advantageous with respect to a low defect rate, with respect to avoiding graphite wall sublimation, and with respect to reducing impurities. A low growth temperature was also found to be favorable with respect to reducing graphitization of the powder source [LCNW03].

Acknowledgments

We thank Olaf Klein, Jürgen Sprekels (WIAS Berlin), Arndt Rösch, Fredi Tröltzsch (TU Berlin), Klaus Böttcher, Detlev Schulz, and Dietmar Siche (IKZ Berlin) for helpful discussions and advice.

References

[BKP+99] N. Bubner, O. Klein, P. Philip, J. Sprekels, and K. Wilmański. *A transient model for the sublimation growth of silicon carbide single crystals.* J. Crystal Growth **205** (1999), 294–304.

[DNR+90] F. Dupret, P. Nicodéme, Y. Ryckmans, P. Wouters, and M.J. Crochet. *Global modelling of heat transfer in crystal growth furnaces.* Intern. J. Heat Mass Transfer **33** (1990), no. 9, 1849–1871.

[FKL01] J. Fuhrmann, Th. Koprucki, and H. Langmach. *pdelib: An open modular tool box for the numerical solution of partial differential equations. Design patterns*, in [pro01].

[Har95] G.L. Harris (ed.). *Properties of Silicon Carbide.* EMIS Datareview Series, no. 13, Institution of Electrical Engineers, INSPEC, London, UK, 1995.

[KDK+01] A.V. Kulik, S.E. Demina, S.K. Kochuguev, D.Kh. Ofengeim, S.Yu. Karpov, A.N. Vorob'ev, M.V. Bogdanov, M.S. Ramm, A.I. Zhmakin, A.A. Alonso, S.G. Gurevich, and Y.N. Makarov. *Inverse-Computation Design of a SiC Bulk Crystal Growth System.* Mat. Res. Soc. Proc. **640** (2001), H1.6.1–H1.6.6.

[Kel99] C.T. Kelley. *Iterative Methods for Optimization.* Siam, Philadelphia, USA, 1999.

[KKZ+00] S.Yu. Karpov, A.V. Kulik, I.A. Zhmakin, Yu.N. Makarov, E.N. Mokhov, M.G. Ramm, M.S. Ramm, A.D. Roenkov, and Yu.A. Vodakov. *Analysis of sublimation growth of bulk SiC crystals in tantalum container.* J. Crystal Growth **211** (2000), 347–351.

[Kon95] A.O. Konstantinov. *Sublimation growth of SiC*, in [Har95], pp. 170–203.

[KP02] O. Klein and P. Philip. *Correct voltage distribution for axisymmetric sinusoidal modeling of induction heating with prescribed current, voltage, or power.* IEEE Trans. Mag. **38** (2002), no. 3, 1519–1523.

[KP03] O. Klein and P. Philip. *Transient numerical investigation of induction heating during sublimation growth of silicon carbide single crystals.* J. Crystal Growth **247** (2003), no. 1–2, 219–235.

[KPSW01] O. Klein, P. Philip, J. Sprekels, and K. Wilmański. *Radiation- and convection-driven transient heat transfer during sublimation growth of silicon carbide single crystals*. J. Crystal Growth **222** (2001), 832–851.

[LCNW03] H. Li, X.L. Chen, D.Q. Ni, and X. Wu. *Factors affecting the graphitization behavior of the powder source during seeded sublimation growth of SiC bulk crystal*. J. Crystal Growth **258** (2003), 100–105.

[MGH+01] St.G. Müller, R.C. Glass, H.M. Hobgood, V.F. Tsvetkov, M. Brady, D. Henshall, D. Malta, R. Singh, J. Palmour, and C.H. Carter Jr. *Progress in the industrial production of SiC substrates for semiconductor devices*. Mater. Sci. Eng. B **80** (2001), no. 1–3, 327–331.

[MZHS03] R.-H. Ma, H. Zhang, S. Ha, and M. Skowronski. *Integrated process modeling and experimental validation of silicon carbide sublimation growth*. J. Crystal Growth **252** (2003), 523–537.

[MZPD02] R. Ma, H. Zhang, V. Prasad, and M. Dudley. *Growth Kinetics and Thermal Stress in the Sublimation Growth of Silicon Carbide*. Crystal Growth & Design **2** (2002), no. 3, 213–220.

[OFK+02] N. Ohtani, T. Fujimoto, M. Katsuno, T. Aigo, and H. Yashiro. *Growth of large high-quality SiC single crystals*. J. Crystal Growth **237–239** (2002), 1180–1186.

[PAC+99] M. Pons, M. Anikin, K. Chourou, J.M. Dedulle, R. Madar, E. Blanquet, A. Pisch, C. Bernard, P. Grosse, C. Faure, G. Basset, and Y. Grange. *State of the art in the modelling of SiC sublimation growth*. Mater. Sci. Eng. B **61-62** (1999), 18–28.

[Phi03] P. Philip. *Transient Numerical Simulation of Sublimation Growth of SiC Bulk Single Crystals. Modeling, Finite Volume Method, Results*. Ph.D. thesis, Department of Mathematics, Humboldt University of Berlin, Germany, 2003, Report No. 22, Weierstraß-Institut für Angewandte Analysis und Stochastik, Berlin.

[pro01] *Proceedings of the 14th GAMM Seminar on Concepts of Numerical Software, Kiel, January 23–25, 1998*. Kiel, Germany, 2001.

[RSD+99] H.-J. Rost, D. Siche, J. Dolle, W. Eiserbeck, T. Müller, D. Schulz, G. Wagner, and J. Wollweber. *Influence of different growth parameters and related conditions on 6H-SiC crystals grown by the modified Lely method*. Mater. Sci. Eng. B **61-62** (1999), 68–72.

[SBP98] N. Schulze, D.L. Barrett, and G. Pensl. *Near-equilibrium growth of mircopipe-free 6H-SiC single crystals by physical vapor transport*. Appl. Phys. Lett. **72** (1998), no. 13, 1632–1634.

[SG03] O. Schenk and K. Gärtner. *Solving Unsymmetric Sparse Systems of Linear Equations*. Journal of Future Generation Computer Systems (2003), in press.

[SGF00] O. Schenk, K. Gärtner, and W. Fichtner. *Scalable Parallel Sparse Factorization with Left-Strategy on Shared Memory Multiprocessor*. BIT **40** (2000), no. 1, 158–176.

[SKM+00] M. Selder, L. Kadinski, Yu. Makarov, F. Durst, P. Wellmann, T. Straubinger, D. Hoffmann, S. Karpov, and M. Ramm. *Global numerical simulation of heat and mass transfer for SiC bulk crystal growth by PVT*. J. Crystal Growth **211** (2000), 333–338.

[SVK+00] A.S. Segal, A.N. Vorob'ev, S.Yu. Karpov, E.N. Mokhov, M.G. Ramm, M.S. Ramm, A.D. Roenkov, Yu.A. Vodakov, and Yu.N. Makarov. *Growth of silicon carbide by sublimation sandwich method in the atmosphere of inert gas*. J. Crystal Growth **208** (2000), 431–441.

[TT78] Yu.M. Tairov and V.F. Tsvetkov. *Investigation of Growth Processes of Ingots of Silicon Carbide Single Crystals*. J. Crystal Growth **43** (1978), 209–212.